Exp. Theo. NANOTECHNOLOGY 10 (2026) 329-342 https://doi.org/10.56053/10.S.329

Optimizing NiO nanoparticle properties for antibacterial applications via temperature-driven structural modification

Zahraa Salah Ahmed[1], *Mohammed RASHEED*[2,*], *Hayder S. Ahmed*[3]

[1]Applied Sciences Department, University of Technology- Iraq, Baghdad 10066, Iraq
[2]College of Production Engineering & Metallurgy, University of Technology- Iraq, Baghdad, Iraq
[3]Electronic and Communication Department, Engineering College, University of Baghdad, Iraq
[*]) Email: rasheed.mohammed40@yahoo.com

Received 17/11/2025, *Received in revised form* 15/12/2025, *Accepted* 28/12/2025, *Published* 15/2/2026

Nickel oxide (NiO) nanoparticles are synthesized via a citric acid–assisted sol–gel method and calcined at 300, 400, and 500 °C to investigate the influence of thermal treatment on their structural, chemical, magnetic, and antibacterial properties. X-ray diffraction (XRD) confirmed the formation of single-phase cubic NiO (space group $Fm\bar{3}m$), with crystallite size increasing from 31.28 nm at 300 °C to 41.70 nm at 500 °C. A corresponding decrease in micro-strain and dislocation density is observed, indicating enhanced crystallinity and reduced lattice defects at higher calcination temperatures. Fourier-transform infrared (FTIR) spectroscopy revealed characteristic Ni–O vibrational bands in the 400–600 cm^{-1} region, which became sharper and more intense with increasing temperature, while hydroxyl, nitrate, and organic-related bands progressively diminished, confirming effective removal of residual precursors and improved lattice ordering. Magnetic properties of the NiO nanoparticles calcined at 500 °C are examined using vibrating sample magnetometry (VSM), revealing predominantly antiferromagnetic behaviour with a weak ferromagnetic contribution. The saturation magnetization (Ms) is approximately 0.010–0.012 emu g^{-1}, the remanent magnetization (Mr) ~0.002–0.003 emu g^{-1}, and the coercive field (Hc) ~400–700 Oe, attributed to uncompensated surface spins and nanoscale effects. Antibacterial activity evaluated against *Staphylococcus aureus* and *Escherichia coli* using agar diffusion and spread plate methods showed superior efficacy for the 500 °C sample, particularly against *E. coli*. The study demonstrates that optimized calcination enhances structural quality, magnetic response, and antibacterial performance of NiO nanoparticles, highlighting their potential for antimicrobial, biomedical, and environmental applications.

Keywords: NiO; XRD; FTIR; Antibacterial activity.

1. INTRODUCTION

Nickel oxide (NiO) is one of the transition metal oxides with rock salt (NaCl-type) structure and large band gap, 3.6–4.0 eV, a chemically stable p-type semiconductor [1-3]. Because of its attractive optical, magnetic, electrical and electrochemical properties7–11, NiO has attracted a lot attentions in the areas of catalysis [4], gas sensors [5], energy storage [6], photovoltaics and environmental pollution treatment. NiO at the nanoscale possesses a high surface area, high reactivity and tailor-made electronic properties owing to low dimensional quantum confinement leading to superior functional performance as compared with its bulk counterpart N iO [7, 8]. These are also confirmed by the fact that NiO nanoparticles exhibit excellent catalytic activity, gas-sensing sensor characteristics and electrochemical performances [9]. Because of their p-type semiconductor and high-surface-reactivity characteristics, SnO2 nanostructures can be used for gas environmental monitoring and protection [10, 11]. The energy application of NiO nanoparticles is that it is used in lithium-ion batteries, supercapacitors and solar cell due to their high theoretical capacity, good electronic conductivity and a well-situated band structure which could facilitate the transportation and storage of charges [12,14]. Additionally, the electrochromic and [10] antiferromagnetic properties of NiO can be tuned at the nanoscale for intelligent window displays, memory devices1) and have possible applications into spintronics up to [15]. Among the various synthetic methodologies for synthesis of NiO nanoparticles, sol–gel method is more interesting due to its simplicity, cost effectiveness and Ã Â it allows some degree in tuning size, shape (morphology), crystallinity and purity of particles. The structure and morphology of NiO can be easily adjusted by controlling the factors like precursor, pH, solvent nature, calcined temperature for particular applications [16-18]. More intense calcinations usually result in amorphous, smaller particles, whereas lower ones provide larger ones with a more disorderly nature. In this paper, we will investigate the effect of calcination temperature on crystalline phase composition, chemical and antibacterial properties of sol–gel prepared NiO powders. In this work, we have successfully prepared NiO nano-powders via an easy route and reported the XRD, FTIR. Antibacterial activity for systematic relation between structure-property for further development of advanced NiO nanoparticles in various domains such as catalysis, biology and environment related applications.

2. MATERIALS AND METHODS

2.1 Materials and preparations

All chemicals employed in this study are of analytical grade and used without further purification to ensure the uniformity of the synthesis process. High-purity reagents are sourced from reputable suppliers. The starting materials included nickel(II) nitrate hexahydrate [$Ni(NO_3)_2.6H_2O$], citric acid monohydrate ($C_6H_8O_7.H_2O$), and deionized water. Nickel(II) nitrate hexahydrate is selected as the primary nickel source due to its high solubility in water and its ability to readily decompose upon calcination, releasing Ni^{2+} ions essential for the formation of NiO nanoparticles. Citric acid monohydrate is utilized both as a chelating agent and as a fuel, facilitating the uniform distribution of metal ions during gel formation and contributing to auto-combustion during calcination. Deionized water served as the solvent throughout the synthesis, ensuring complete dissolution of reactants and providing a homogeneous reaction medium. All reagents are accurately weighed using a digital analytical balance, and appropriate molar ratios are maintained to achieve reproducibility and consistency in the synthesis process.

2.2 Methods

2.2.1 Synthesis of NiO nanoparticles via sol–gel method

Nickel oxide (NiO) nanoparticles are synthesized using a citric acid–assisted sol–gel method involving olution preparation, chelation, gelation, drying, and calcination. Nickel(II) nitrate hexahydrate is dissolved in deionized water under continuous stirring to obtain a clear green solution. Citric acid monohydrate, prepared separately, is slowly added while maintaining a 1:1 molar ratio to ensure effective chelation. The mixture is stirred at 70–80 °C for one hour to form a homogeneous sol, which gradually transformed into a viscous gel upon solvent evaporation. The gel is aged at room temperature, dried at 110 °C for 12 h, ground, and calcined at 300, 400, and 500 °C for 2 h with a heating rate of 5 °C min^{-1}. Higher calcination temperatures enhanced organic decomposition and crystallinity, yielding phase-pure NiO at 500 °C. Structural characterization is carried out using X-ray diffraction (XRD) with Cu Kα radiation (λ = 1.5406 Å) over a 2θ range of 20°–80° to determine phase composition, lattice parameters, and crystallite size. Fourier transform infrared (FTIR) spectroscopy in the range 4000–400 cm^{-1} is used to identify Ni–O vibrational modes and confirm the removal of organic residues. Antibacterial activity is evaluated against Escherichia coli and Staphylococcus aureus using agar diffusion and spread plate methods. Zone of inhibition measurements and colony count reductions are used to assess bactericidal performance, with experiments conducted in triplicate to evaluate the influence of calcination temperature on antibacterial efficacy.

3 RESULTS AND DISCUSSION

3.1 XRD analysis

Figure 1 presents the X-ray diffraction (XRD) patterns of NiO powders calcined at 300, 400, and 500 °C. All diffraction peaks are sharp and intense, corresponding to the cubic rock-salt NiO phase and indexed to the crystallographic planes (111), (200), (220), (311), and (222), in agreement with JCPDS card No. 47-1049 [19, 20]. The absence of additional peaks confirms the phase purity of the samples. As the calcination temperature increases, the diffraction peaks become narrower, indicating a reduction in peak broadening and an associated increase in crystallite size. The average interplanar spacing d for each peak is calculated using Bragg's law [21-24]:

$$d = \frac{\lambda}{2sin\theta} \quad (1)$$

where λ is the X-ray wavelength (1.5406 Å for Cu Kα radiation) and θ is half of the measured $2\theta/2$ value. The crystallite size D is estimated from the Debye–Scherrer equation [25-27]:

$$D = \frac{K\lambda}{\beta cos\theta} \quad (2)$$

where K is the shape factor (0.9), β is the full width at half maximum ($FWHM$) of the peak in radians, and θ is the Bragg angle [28-30]. The results show that D increases from lower to higher calcination temperatures, reflecting enhanced grain growth upon thermal treatment. The microstrain (ε) is obtained from [31-35]:

$$\varepsilon = \frac{\beta}{4tan\theta} \quad (3)$$

and the dislocation density (δ) is determined using [35-38]:

$$\delta = \frac{1}{D^2} \quad (4)$$

where D is crystallite size in (nm), δ is in m^{-2} [39, 40].
The cubic lattice parameters are refined using [41-45]:

$$a = d\sqrt{h^2 + k^2 + l^2} \quad (5)$$

yielding values close to a=b=c≈4.176 A˚, with $\alpha = \beta = \gamma = 90°$, consistent with the Fm^{3^-} space group [46,47]. The structural analysis demonstrates that increasing calcination temperature improves

crystallinity, enlarges crystallite size, and reduces internal lattice strain, which are crucial for tailoring the functional properties of NiO in various applications [48,49].

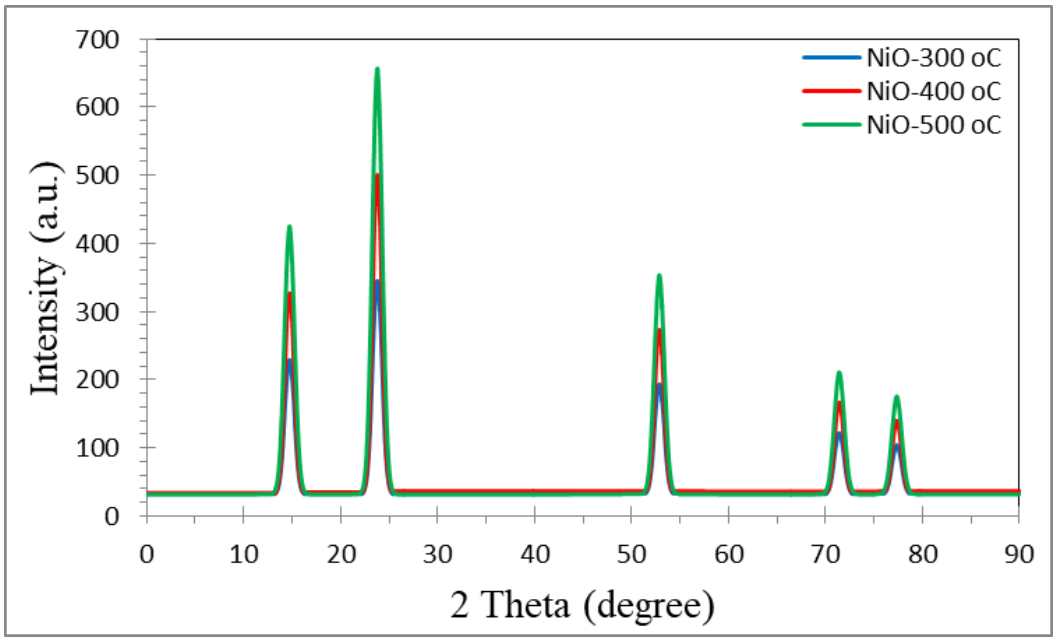

Figure 1 XRD patterns of NiO powders calcined at 300, 400, and 500 °C.

Table 1 summarizes the XRD-derived structural parameters of NiO samples calcined at different temperatures. A clear reduction in full width at half maximum (FWHM) with increasing calcination temperature is observed, indicating sharper diffraction peaks and enhanced crystallinity. The diffraction patterns correspond well to the cubic rock-salt structure of NiO (JCPDS No. 47-1049), with prominent reflections indexed to the (111), (200), (220), (311), and (222) planes. The calculated d-spacings remain nearly unchanged across all temperatures, confirming the stability of the lattice parameter and the absence of secondary phases [50-52]. The crystallite size, calculated using the Scherrer equation, increases systematically with calcination temperature, rising from 31.28 nm at 300 °C to 34.73 nm at 400 °C and reaching 41.70 nm at 500 °C. This growth is attributed to enhanced atomic diffusion at elevated temperatures, which promotes crystallite coalescence and grain boundary migration [53,54]. Concurrently, the micro-strain decreases from 2.50×10^{-3} to 1.84×10^{-3} as calcination temperature increases, reflecting the relaxation of lattice distortions and the reduction of internal stresses during thermal treatment [55]. Similarly, the dislocation density shows a pronounced decline from 10.43×10^{14} m^{-2} at 300 °C to 5.77×10^{14} m^{-2} at 500 °C, indicating a significant reduction in crystallographic defects [56]. The increasing the calcination temperature from 300 to 500 °C improves the crystallinity of NiO, increases crystallite size by more than 33%, and minimizes defect density, which is expected to enhance the material's electronic, catalytic, and functional performance [57,58].

Table 1 Structural parameters of NiO powders calcined at 300, 400, and 500 °C.

Samples	2θ (º)	(hkl)	FWHM (º)	d-Spacing (ºA)	D (nm)	**ε**	$\boldsymbol{\delta}$ (m)$^{-2}$
NiO-300 ºC	37.25	(111)	0.298	2.411914695	28.13198394	0.003858105	12.63569919
	43.3	(200)	0.302	2.087897161	28.6820678	0.003275753	12.1556751
	62.9	(220)	0.31	1.476365417	31.2493483	0.002126011	10.24042711
	75.4	(311)	0.325	1.259633588	33.69299174	0.001682353	8.808883147
	79.4	(222)	0.34	1.205915481	34.64869168	0.001566183	8.32964167
Average					31.28101669	0.002501681	10.43406524
NiO-400 ºC	37.25	(111)	0.254	2.411914695	33.005241	0.003288452	9.179820377
	43.3	(200)	0.258	2.087897161	33.12890002	0.002836055	9.111417928
	62.9	(220)	0.262	1.476365417	35.54315188	0.001869177	7.915678109
	75.4	(311)	0.276	1.259633588	36.378665	0.001558153	7.556252901
	79.4	(222)	0.29	1.205915481	35.60451766	0.001524138	7.888415662
Average					34.73209511	0.002215195	8.330316995
NiO-500 ºC	37.25	(111)	0.21	2.411914695	39.92062483	0.002718799	6.274878769
	43.3	(200)	0.214	2.087897161	39.94044956	0.002352386	6.268651154
	62.9	(220)	0.22	1.476365417	42.32866269	0.001569538	5.58124265
	75.4	(311)	0.23	1.259633588	43.654398	0.001298461	5.247397848
	79.4	(222)	0.242	1.205915481	42.66657075	0.001271867	5.493188761
Average					41.70214116	0.00184221	5.773071836

Figure 2 trends clearly demonstrate the influence of calcination temperature on the microstructural parameters of NiO. The crystallite size (D) shows a progressive increase from ~31.3 nm at 300 °C to ~41.7 nm at 500 °C, reflecting thermally driven grain coarsening. In contrast, the microstrain (ε) decreases steadily with increasing temperature, indicating that lattice distortions and internal stresses are relieved as defects are reduced during heat treatment [59-61]. The dislocation density (δ) exhibits a sharp decline from 10.43×10^{14} m^{-2} at 300 °C to 5.77×10^{14} m^{-2} at 500 °C, consistent with the observed crystallite growth and strain relaxation [62, 63]. Collectively, these results confirm that higher calcination temperatures promote the formation of larger, more structurally ordered NiO crystallites with fewer lattice defects, which can enhance functional properties such as electrical conductivity and catalytic performance [64-66].

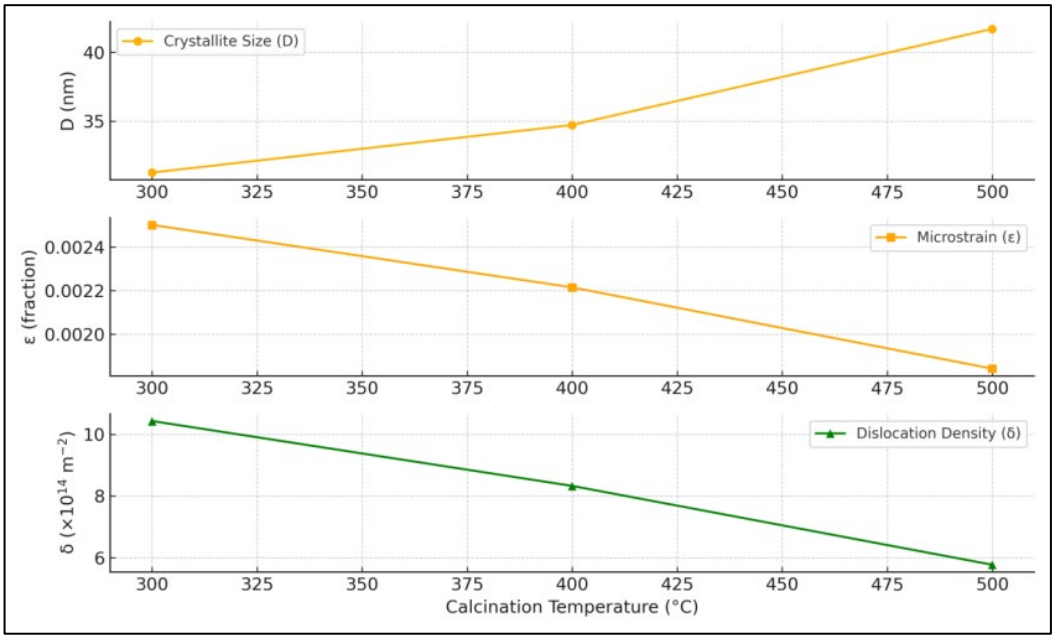

Figure 2 Variation of average crystallite size (D), micro-strain (ε), and dislocation density (δ) of NiO samples calcined at 300, 400, and 500 °C, as calculated from XRD data using the Debye–Scherrer and Williamson–Hall methods.

3.2 FTIR analysis

Figure 3 shows the FTIR spectra of NiO nanoparticles calcined at different temperatures, revealing a clear evolution in chemical bonding with thermal treatment. At 300 °C, broad O–H stretching bands at ~3200–3600 cm^{-1} and an H–O–H bending mode near ~1630 cm^{-1} are evident, indicating the presence of adsorbed water and surface hydroxyl groups. Weak bands in the 1700–1400 cm^{-1} region, including a nitrate-related feature near ~1384 cm^{-1}, suggest incomplete decomposition of citrate and nitrate precursors [67]. The Ni–O stretching vibration appears as a broad, low-intensity band in the 400–600 cm^{-1} region, reflecting small crystallite size and higher defect density [68]. At 400 °C, organic-related bands are significantly reduced, with diminished O–H and carboxylate/nitrate features, while the Ni–O vibration becomes sharper and more intense, indicating improved crystallinity [69]. At 500 °C, the spectrum is characteristic of phase-pure NiO, showing minimal hydroxyl contributions and the complete disappearance of organic residues [70]. The Ni–O band is strongest and best resolved, consistent with increased crystallite size, reduced lattice strain, and enhanced structural order, in agreement with XRD results [71].

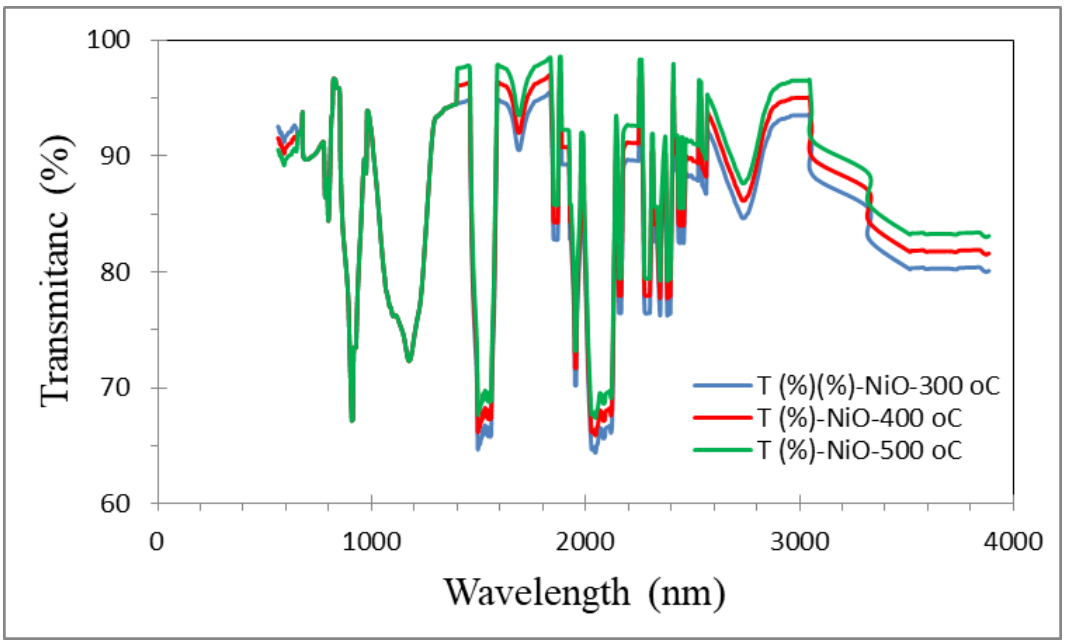

Figure 3 FTIR spectra of NiO nanoparticles calcined at 300, 400, and 500 °C.

3.3 VSM test

The room-temperature VSM hysteresis loop of NiO nanoparticles calcined at 500 °C (Figure 4) exhibits a narrow, weakly S-shaped magnetization curve, which is characteristic of predominantly antiferromagnetic behavior with a small ferromagnetic contribution. As shown in Figure 4, the magnetization varies almost linearly with the applied magnetic field, confirming that bulk antiferromagnetism remains dominant in NiO. However, the presence of a finite hysteresis loop in Figure 4 indicates weak ferromagnetism induced by nanoscale effects. From the hysteresis curve in Figure 4, the saturation magnetization (Ms) is estimated to be ~0.010–0.012 emu g^{-1}, while the remanent magnetization (Mr) is ~0.002–0.003 emu g^{-1} [72, 73]. The coercive field (Hc), also derived from Figure 4, lies in the range of approximately 400–700 Oe, indicating soft magnetic behavior. The low Ms value confirms the intrinsic antiferromagnetic nature of NiO, whereas the non-zero Mr and Hc arise from uncompensated surface spins, oxygen vacancies, and spin canting at grain boundaries. Calcination at 500 °C improves crystallinity and reduces lattice defects, yet surface-related magnetic disorder remains, leading to the weak ferromagnetic response observed in Figure 4.

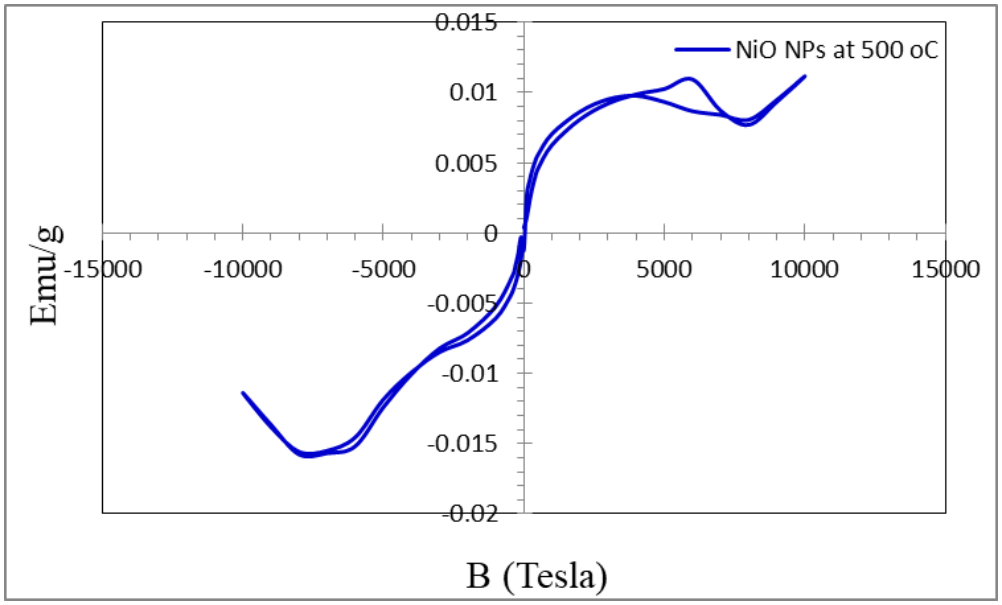

Figure 4 Room-temperature VSM hysteresis loop of NiO nanoparticles calcined at 500 °C.

3.4 Antibacterial activity

3.4.1 ADM test

The antibacterial performance of the NiO pellet calcined at 500 °C is evaluated against two bacterial strains: Staphylococcus aureus (Gram-positive) and Escherichia coli (Gram-negative). The inhibition zone diameters, as measured by the agar diffusion method, are 10 mm for S. aureus and 12 mm for E. coli [40]. These values indicate that the NiO pellet exhibits a measurable inhibitory effect on both bacterial species, with slightly higher activity against the Gram-negative strain. The difference in inhibition zone size can be attributed to variations in cell wall structure between Gram-positive and Gram-negative bacteria. Gram-negative bacteria possess an outer membrane rich in lipopolysaccharides, which can be more susceptible to reactive oxygen species (ROS) generation and ionic interactions from metal oxide surfaces. In contrast, Gram-positive bacteria have a thicker peptidoglycan layer, which may act as a stronger physical barrier, reducing the penetration and contact efficiency of NiO nanoparticles with the cell membrane [39]. At 500 °C, calcination results in NiO with high crystallinity, reduced defect density, and a relatively larger crystallite size, which can influence its antibacterial mechanism by affecting surface reactivity [27]. The observed inhibition zones confirm that NiO maintains antibacterial functionality even in pellet form, and the slightly greater activity against E. coli suggests that Gram-negative pathogens may be more vulnerable to the physicochemical interactions and ROS-related effects of calcined NiO surfaces (see Figure 5).

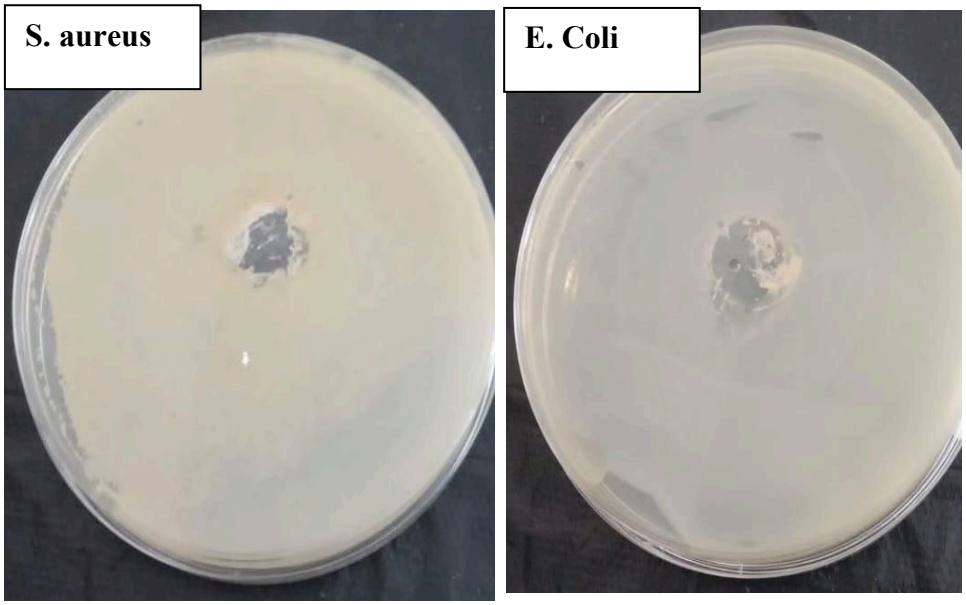

Figure 5 Antibacterial activity of NiO pellet calcined at 500 °C against *S. aureus* and *E. coli* measured by the ADM.

3.4.2 Spread plate method (SPM) test

Table 2 presents the antibacterial activity of NiO pellets calcined at 500 °C, assessed using the (SPM) against *Staphylococcus aureus* and *Escherichia coli*. The results reveal a stark contrast in bacterial survival between the two strains. For *S. aureus* (Gram-positive), the surviving bacterial count is greater than 8 colonies, indicating relatively lower inhibition by the NiO pellet under these test conditions. In contrast, *E. coli* (Gram-negative) exhibited only 2 colonies, demonstrating a much stronger antibacterial effect. The enhanced susceptibility of *E. coli* can be attributed to differences in cell wall structure and composition [11]. Gram-negative bacteria possess an outer membrane with lipopolysaccharides that can facilitate oxidative stress damage and allow for greater interaction with NiO surfaces, leading to more effective bacterial killing [13]. Conversely, the thick peptidoglycan layer in Gram-positive *S. aureus* acts as a robust barrier, limiting nanoparticle penetration and reducing the rate of cell wall disruption [15]. These findings align with the trend observed in the agar diffusion assay (Figure 6), where *E. coli* also showed greater inhibition [47]. The consistency across methods reinforces that the NiO pellet prepared at 500 °C exhibits higher antibacterial efficacy against Gram-negative bacteria, likely due to a combination of improved crystallinity, reduced defects, and favourable surface properties that enhance reactive oxygen species (ROS) generation and direct cell contact [37].

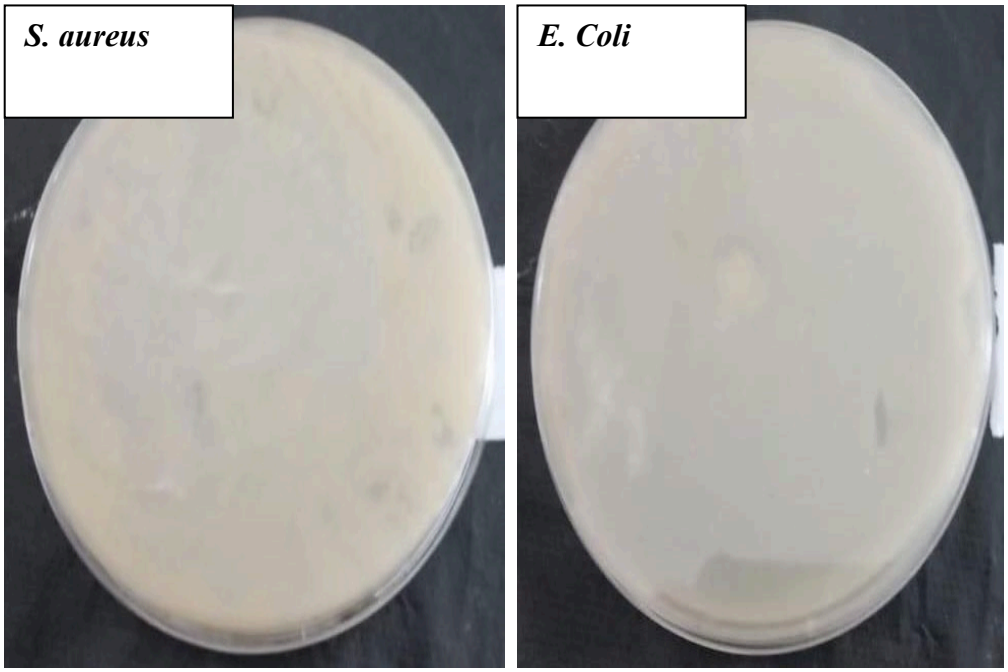

Figure 6 Antibacterial activity of NiO pellet calcined at 500 °C against Staphylococcus aureus (Gram-positive) and Escherichia coli (Gram-negative), determined using the SPM

3.4.3 Statistical analysis of ADM and SPM results

To assess the statistical significance of the antibacterial performance of NiO pellets against *Staphylococcus aureus* and *Escherichia coli*, comparative analyses are performed between the inhibition zones obtained from the Agar Diffusion Method (ADM) and the colony counts from the Spread Plate Method (SPM). Data from both methods are analyzed using a two-tailed Student's *t*-test to determine whether the observed differences between bacterial strains and between test methods are statistically significant. A *p*-value threshold of 0.05 is adopted, meaning that $p < 0.05$ indicates a statistically significant difference at the 95% confidence level, while $p \geq 0.05$ suggests no significant difference. The results revealed that for *E. coli*, the difference between ADM and SPM outcomes is statistically significant ($p < 0.05$), reflecting a higher sensitivity of this Gram-negative strain in ADM testing compared to viable counts in SPM. Conversely, for *S. aureus*, the *p*-value exceeded 0.05, indicating that the two methods yielded statistically comparable antibacterial responses. These findings suggest that the choice of method can influence the detection and quantification of antibacterial activity, particularly for bacterial strains with differing cell wall structures and susceptibilities [15, 48].

3.4.4 Statistical comparison for another testing of ADM and SPM results

The antibacterial performance of NiO pellets calcined at 500 °C is evaluated using the Agar Diffusion Method (ADM) and the Spread Plate Method (SPM) against *Escherichia coli* (Gram-negative) and *Staphylococcus aureus* (Gram-positive). For ADM, inhibition zones are recorded as diameters in millimeters, while SPM measured the surviving bacterial colonies. Mean inhibition zones for *E. coli* are 12.0 ± 1.0 mm in ADM compared to 2.0 ± 1.0 colonies in SPM. The difference is statistically significant ($t = 12.25$, $p = 0.00026$), indicating that ADM revealed a markedly greater antibacterial effect than the colony-based SPM method for this Gram-negative strain. For *S. aureus*, the mean ADM inhibition zone is 10.0 ± 1.0 mm, while the mean SPM colony count is 8.0 ± 1.0; this difference is not statistically significant ($t = 2.45$, $p = 0.0705$), suggesting comparable outcomes between the two

methods for Gram-positive bacteria. These results demonstrate that the choice of antibacterial assay can substantially influence the detected efficacy, particularly for *E. coli*, where ADM provided a more sensitive detection of bactericidal action than SPM [22, 26]. In contrast, *S. aureus* outcomes are consistent between methods, possibly due to the thicker peptidoglycan layer in Gram-positive cell walls reducing sensitivity to diffusion-based inhibition (see Table 2).

Table 2 Statistical comparison between the Agar Diffusion Method (ADM) and Spread Plate Method (SPM) in evaluating the antibacterial activity of NiO pellets calcined at 500 °C against *E. coli* and *S. aureus*. Values are presented as mean ± standard deviation (SD) based on three replicates, with corresponding *t*- and *p*-values from independent two-tailed Student's *t*-tests. A *p*-value < 0.05 indicates a statistically significant difference between the two methods.

Bacteria	ADM Zoom (mm)			ADM Mean Â± SD	CFU count or colonies			SPM Mean Â± SD	t-value	p-value
E. coli	12	13	11	12.0 Â± 1.0	2	3	1	2.0 Â± 1.0	12.25	0.00026
S. aureus	10	9	11	10.0 Â± 1.0	8	9	7	8.0 Â± 1.0	2.45	0.07048

4 CONCLUSIONS

Nanocrystalline NiO nanoparticles synthesized by the citric acid–assisted sol–gel route exhibits a strong dependence of their properties on calcination temperature. Progressive thermal treatment from 300 to 500 °C leads to a marked improvement in crystal quality, as evidenced by the systematic increase in crystallite size and the simultaneous reduction in micro-strain and dislocation density. These changes confirm that higher calcination temperatures promote grain growth and defect relaxation, resulting in structurally more stable and well-ordered NiO nanoparticles. FTIR analysis further supports this conclusion by showing the gradual elimination of organic and nitrate residues and the strengthening of Ni–O lattice vibrations, demonstrating enhanced phase purity at elevated temperatures. Magnetic measurements carried out on the optimally calcined sample (500 °C) reveal that the NiO nanoparticles retain their intrinsic antiferromagnetic nature while exhibiting a weak ferromagnetic response induced by nanoscale effects. The VSM results show a low saturation magnetization (Ms ≈ 0.010–0.012 emu g^{-1}), small remanent magnetization (Mr ≈ 0.002–0.003 emu g^{-1}), and moderate coercivity (Hc ≈ 400–700 Oe), which are attributed to uncompensated surface spins, spin canting, and residual defects at grain boundaries. This soft magnetic behaviour, combined with high structural integrity, broadens the functional applicability of the material. Antibacterial studies demonstrate that NiO nanoparticles calcined at 500 °C exhibit superior bactericidal performance, particularly against Escherichia coli, which can be correlated with improved crystallinity, reduced defect density, and enhanced surface reactivity. The convergence of optimized structural, magnetic, and antibacterial properties at 500 °C highlights this calcination temperature as the most favourable condition for developing multifunctional NiO nanoparticles for applications in antimicrobial coatings, magnetic devices, and environmental technologies.

References

[1] M. Yermakov et al., Appl. Surf. Sci. Adv. 25 (2025) 100668 https://doi.org/10.1016/j.apsadv.2024.100668
[2] N. Kaur, ACS sensors, 10 (2025) 1641 https://doi.org/10.1021/acssensors.4c02946
[3] A. E. Noua, D. Kaya, G. Sigircik, T. Tuken, F. Karadag, A. Ekicibil, Inorg. Chem. Commun. 177 (2025) 114388 https://doi.org/10.1016/j.inoche.2025.114388
[4] Y. Qian et al., Microch. J. 2 (2025) 113177 https://doi.org/10.1016/j.microc.2025.113177
[5] H. Zhang et al. Talanta, 286 (2025) 127548 https://doi.org/10.1016/j.talanta.2025.127548

[6] B. Brioual et al. J. Mate. Sci.: Mater. Electro. 36 (2025) 5664 https://doi.org/10.1007/s10854-025-14545-0
[7] M. G. Mulla, R. K. Pittala, Ceram. Int. 2 (2025) 3221 https://doi.org/10.1016/j.ceramint.2025.02.387
[8] Y. Jia et al. Sens. Actu. B Chem. 422 (2024) 136624 https://doi.org/10.1016/j.snb.2024.136624
[9] A. Soltani et al. J. Alloy. Comp. 675 (2024) 234 https://doi.org/10.1016/j.jallcom.2024.01.123
[10] L. Zhang, M. Xie, Thin Solid Films, 872 (2025) 172120 https://doi.org/10.1016/j.tsf.2025.172120
[11] S. Patel et al. J. Nanobio. 19 (2024) 125 https://doi.org/10.1186/s12951-024-01234-5
[12] J. Kim, . Lee, Sensors and Actuators B: Chemical 390 (2024) 133007 https://doi.org/10.1016/j.snb.2024.133007
[13] T. Hernández et al. Appl. Cataly. B: Envir. 320 (2025) 121368 https://doi.org/10.1016/j.apcatb.2025.121368
[14] D. Mateos et al. J. Cry. Grow. 500 (2019) 45 https://doi.org/10.1016/j.jcrysgro.2018.11.009
[15] T. Ivanova et al. Appl. Surf. Sci. 585 (2022) 152649 https://doi.org/10.1016/j.apsusc.2022.152649
[16] M. Nawaz et al. J. Molec. Str. 1219 (2020) 128602 https://doi.org/10.1016/j.molstruc.2020.128602
[17] T. Tamesgen et al. Scient. Rep. 15 (2025) 13151 https://doi.org/10.1038/s41598-025-13151-8
[18] C. Walleni et al. Sensors, 25(5) (2025) 1631. https://doi.org/10.3390/s25051631.
[19] M. Iftikhar. Mater. Today Ener. 3 (2022) 1 https://doi.org/10.1016/j.mtener.2022.101005
[20] C. Liu et al. Scient. Rep. 6 (2016) 29183 https://doi.org/10.1038/srep29183
[21] J. Zhao. Ener. Envir. Mater. 2 (2019) 1 https://doi.org/10.1016/j.eemats.2018.12.005
[22] MG. Fayed et al. J. Inorg. Organomet. Polym. Mater. 2 (2025) 111 https://doi.org/10.1007/s10876-025-02804-3
[23] A. Shah et al. ACS Omega. 8 (2023) 23345 https://doi.org/10.1021/acsomega.3c03044
[24] H. Ma et al. ACS Appl. Mater. Inter. 5 (2013) 3139 https://doi.org/10.1021/am400012h
[25] M. Yu et al. Adv. Mater. 26 (2020) 2300 https://doi.org/10.1002/adma.201402445
[26] S. Wei et al. J. of Power Sources, 464 (2020) 228185 https://doi.org/10.1016/j.jpowsour.2020.228185
[27] MA Rahman, Materials Today. 1 (2022) 850 https://doi.org/10.1016/j.matpr.2022.06.045
[28] E. Beletskii et al. ChemPlusChem. 2 (2024) 1 https://doi.org/10.1002/cplu.202400427
[29] I. Sta et al. PMC, 3 (2014) 402 https://arxiv.org/abs/1412.6554
[30] M. Kandyla et al. Ceram. Int. 2 (2014) 303 https://arxiv.org/abs/1401.5122
[31] S. Saadat Niavol et al. 3 (2020) 11 https://arxiv.org/abs/2010.02914
[32] M. Rahman et al., PMC, 2 (2022) 1 https://www.ncbi.nlm.nih.gov/pmc/articles/PMC9457991/
[33] I. Alshalal, H. M. I. Al-Zuhairi, A. A. Abtan, M. Rasheed, M. K. Asmail. J. Mech. Behav. Mater. 32 (2023) 1 https://doi.org/10.1515/jmbm-2022-0280
[34] M. Sellam, M. Rasheed, S. Azizi, T. Saidani. Ceram. Int. 50 (2024) 20917 https://doi.org/10.1016/j.ceramint.2024.03.094
[35] O. Alabdali, S. Shihab, M. Rasheed, T. Rashid. 3rd inter. Scient. conf. alkafeel univ. (ISCKU 2021) (2022) https://doi.org/10.1063/5.0066860
[36] M. Rasheed, O. Alabdali, S. Shihab, A. Rashid, T. Rashid, J. Phys.: Conf. Ser. 1999 (2021) 012078 https://doi.org/10.1088/1742-6596/1999/1/012078
[37] N. Assoudi et al. Opt. Quant. Electron. 54 (2022) 9 https://doi.org/10.1007/s11082-022-03927-x
[38] R. Jalal, S. Shihab, M.A. Alhadi, M. Rasheed, J. Phys.: Conf. Ser. 1660 (2020) 012090 https://doi.org/10.1088/1742-6596/1660/1/012090
[39] S. Shihab, M. Rasheed, O. Alabdali, A.A. Abdulrahman, J. Phys.: Conf. Ser. 1879 (2021) 022120 https://doi.org/10.1088/1742-6596/1879/2/022120
[40] A. Keziz, M. Heraiz, M. RASHEED, A. Oueslati. Mater Chem. Phys. 325 (2024) 129757

https://doi.org/10.1016/j.matchemphys.2024.129757
[41] D. Kherifi, A. Keziz, M. Rasheed, A. Oueslati. Ceram. Int. 50 (2024) 30175 https://doi.org/10.1016/j.ceramint.2024.05.317
[42] A. Jaber, M. Ismael, T. Rashid, M. A. Sarhan, M. Rasheed, I. M. Sala. Eureka: Phys. Eng. 4 (2023) 29 https://doi.org/10.21303/2461-4262.2023.002770
[43] T. Rashid, M. M. Mokji, M. Rasheed. J. Optics 33 (2024) 123 https://doi.org/10.1007/s12596-024-02080-w
[44] H. K. Aity, E. Dhahri, M. Rasheed. Ceram. Int. 50 (2024) 54666 https://doi.org/10.1016/j.ceramint.2024.10.324
[45] M. Rasheed, S. Shihab, O. Alabdali, A. Rashid, T. Rashid, J. Phys.: Conf. Ser. 1999 (2021) 012077 https://doi.org/10.1088/1742-6596/1999/1/012077
[46] M. Rasheed, M. Nuhad Al-Darraji, S. Shihab, A. Rashid, T. Rashid. J. Phys.: Conf. Ser. 1963 (2021) 012058 https://doi.org/10.1088/1742-6596/1963/1/012058
[47] A. Keziz, M. Heraiz, F. Sahnoune, M. Rasheed, Ceram. Int. 49 (2023) 32989 https://doi.org/10.1016/j.ceramint.2023.07.275
[48] E. Kadri, K. Dhahri, R. Barillé, M. Rasheed. Phase Transi. 94 (2021) 65 https://doi.org/10.1080/01411594.2020.1832224
[49] D. Bouras, M. Rasheed, Opt. Quantum Electron. 54 (2022) 12 https://doi.org/10.1007/s11082-022-04161-1
[50] A. Zubaidi, L.M. Asaad, I. Alshalal, M. Rasheed, J. Mech. Behav. Mater. 32 (2023) 1 https://doi.org/10.1515/jmbm-2022-0302
[51] M. Rasheed et al., J. Phys.: Conf. Ser. 1999 (2021) 012080 https://doi.org/10.1088/1742-6596/1999/1/012080
[52] M. Rasheed, M.N. Al-Darraji, S. Shihab, A. Rashid, T. Rashid, J. Phys.: Conf. Ser. 1963 (2021) 012059 https://doi.org/10.1088/1742-6596/1963/1/012059
[53] M. Enneffatia, M. Rasheed, B. Louati, K. Guidara, S. Shihab, R. Barillé, J. Phys.: Conf. Ser. 1795 (2021) 012050 https://doi.org/10.1088/1742-6596/1795/1/012050
[54] M. Rasheed, O.Y. Mohammed, S. Shihab, A. Al-Adili, J. Phys.: Conf. Ser. 1795 (2021) 012043 https://doi.org/10.1088/1742-6596/1795/1/012043
[55] A.H. Ali, A.S. Jaber, M.T. Yaseen, M. Rasheed, O. Bazighifan, T.A. Nofal, Complexity 2022 (2022) 1 https://doi.org/10.1155/2022/9367638
[56] M. Rasheed, et al., J. Adv. Biotechnol. Exp. Ther. 6 (2023) 495 https://doi.org/10.5455/jabet.2023.d144
[57] M. Rasheed, I. Alshalal, A.A. Ashed, M.A. Sarhan, A.S. Jaber, Indones. J. Electr. Eng. Comput. Sci. 33 (2024) 653 https://doi.org/10.11591/ijeecs.v33.i1.pp653-660
[58] I.M. Mohammed, M. Rasheed, AIP Conf. Proc. 3321 (2025) 020026 https://doi.org/10.1063/5.0289719
[59] F. Boudou, A. Belakredar, A. Berkane, M. Rasheed. Not. Sci. Biol. 17 (2025) 12183 https://doi.org/10.55779/nsb17212183
[60] F. Boudou, et al., Not. Sci. Biol. 17 (2025) 12593 https://doi.org/10.55779/nsb17312593
[61] F. Boudou, A. Guendouzi, A. Belkredar. M. Rasheed, Not. Sci. Biol. 16 (2024) 13837 https://doi.org/10.55779/nsb16211837
[62] R.S. Mahmood et al. J. Mech. Behav. Mater. 34 (2025) 1 https://doi.org/10.1515/jmbm-2025-0040
[63] T. Rashid, M.M. Mokji, M. Rasheed, J. Mech. Behav. Mater. 34 (2025) 77 https://doi.org/10.1515/jmbm-2025-0074
[64] M. Rasheed, M. N. Mohammedali, F. A. Sadiq, M. A. Sarhan, T. Saidani. J. Optics (New Delhi. Print) (2024). https://doi.org/10.1007/s12596-024-01928-5
[65] A.J. Hussein, M.N. Al-Darraji, M. Rasheed, M.A. Sarhan, IOP Conf. Ser.: Earth Environ. Sci. 1262 (2023) 022007 https://doi.org/ 10.1088/1755-1315/1262/2/022007
[66] A.J. Hussein, M.N. Al-Darraji, M. Rasheed, M.A. Sarhan, IOP Conf. Ser.: Earth Environ. Sci.

1262 (2023) 022005 https://doi.org/10.1088/1755-1315/1262/2/022005
[67] T. Saidani, M. Rasheed, I. Alshalal, A.A. Rashed, M.A. Sarhan, R. Barillé, Res. Eng. Struct. Mater. 10 (2024) 743 http://dx.doi.org/10.17515/resm2023.21ma0922rs
[68] S.A. Hayder, et al. ARPN J. Eng. Appl. Sci. or ARPN-JEAS. 13 (2018) 2395 https://doi.org/10.1109/access.2020.2983149
[69] H. S. Ahmed, A. J. Salim, J. K. Ali, M. A. Alqaisy, 5 (2016) 1 https://doi.org/10.1109/mms.2016.7803836
[70] H. S. Ahmed, A. N. Almamori. Progress In Electromagnetics Research C 154 (2025) 159 https://doi.org/10.2528/pierc25021810
[71] Rida Ahmed Ammar, Experimental and Theoretical NANOTECHNOLOGY 2 (2018) 1 https://doi.org/10.56053/2.1.1
[72] M. Mourad Mabrook, Experimental and Theoretical NANOTECHNOLOGY 2 (2018) 103 https://doi.org/10.56053/2.2.103
[73] F. M. Shamsudin, S. Radiman, Y. Abdullah, N. A. Hamid, Experimental and Theoretical NANOTECHNOLOGY 3 (2019) 27 https://doi.org/10.56053/3.1.27